On suitability of phase-field and algebraic volume-of-fluid OpenFOAM® solvers for gas-liquid microfluidic applications

F. Jamshidi[a,§,1], H. Heimel[b,c,§], M. Hasert[c], X. Cai[d], O. Deutschmann[d], H. Marschall[e] and M. Wörner[a,*]

[a]*Karlsruhe Institute of Technology (KIT), Institute of Catalysis Research and Technology, Engesserstr. 20, 76131 Karlsruhe, Germany*

[b]*University of Freiburg, Department of Microsystems Engineering – IMTEK, Georges-Koehler-Allee 103, D-79110 Freiburg, Germany*

[c]*Festo AG & Co. KG, CR-CP Department, Computer Aided Engineering Projects, Ruiter Straße 82, 73734 Esslingen, Germany*

[d]*Karlsruhe Institute of Technology (KIT), Institute for Chemical Technology and Polymer Chemistry, Engesserstr. 20, 76131 Karlsruhe, Germany*

[e]*Technische Universität Darmstadt, Mathematical Modeling and Analysis, Dep. of Mathematics, 64287 Darmstadt, Germany*

§ These authors contributed equally to this work

1 Present address: Hochschule Karlsruhe - Technik und Wirtschaft, Institut für Digitale Materialforschung (IDM), Willy-Andreas-Allee 19, 76133 Karlsruhe, Germany

* Corresponding author, E-mail: martin.woerner@kit.edu, Phone +49 721 608-47426, ORCID: 0000-0003-4630-9292

Abstract

Microfluidic devices often contain several phases. Their design can be supported by interface-resolving numerical simulations, requiring accurate methods and validated computer codes. Especially challenging are submillimetre air bubbles in water due to their large density contrast and dominance of surface tension. Here, we evaluate two numerical methods implemented in OpenFOAM®, namely the standard solver `interFoam` with an algebraic volume-of-fluid method relying on a sharp interface representation and `phaseFieldFoam` relying on the phase-field method with diffuse interface representation. For a circular bubble in static equilibrium, we explore the impacts of uniform grid resolution and bubble size on bubble shape, mass conservation, pressure jump and spurious currents. While the standard `interFoam` solver exhibits excellent mass conservation with errors below 0.1% on fine grids, it lacks the accuracy to predict reasonable physics for a bubble in microfluidic systems. At higher resolution, large spurious currents significantly displace and deform the bubble, which is oscillating with resolution dependent mode and frequency. Furthermore, the pressure jump is consistently underestimated by more than 10%. The solver `phaseFieldFoam` suffers from much larger mass losses of up to 2%, which decrease as the ratio between interface thickness and bubble diameter decreases provided the diffuse interface region is adequately resolved. Spurious currents are very low and the bubble remains circular preserving its initial position with an error in pressure jump below 1%.

Keywords: multiphase microfluidics, volume-of-fluid method, phase-field method, OpenFOAM®, spurious currents, surface tension model

1   Introduction

Dispersed multiphase flows in microfluidics continue to pave the way towards laboratory automation, decreasing sample analysis times at minimum fluid expenditure [1]. Using droplets as micro reaction chambers in the medical and biochemical field is one key application [2, 3]. While such droplets are purposely produced, the undesired emergence of gas bubbles is a common problem severely impairing the functionality of microfluidic devices [4]. Adverse effects range from larger bubbles clogging channels [5, 6] to smaller bubbles pinning to channel walls disturbing the flow. While mechanisms for removing bubbles in microfluidic circuits are studied thoroughly [7-9], for designing microfluidic devices accurate numerical simulations on bubble transport and adhesion processes are desirable.

Microfluidic multiphase flows are dominated by interface phenomena due to spatial scaling. Important effects include the thin liquid film between moving gas bubbles and a solid wall [10-12], contact angle dynamics [13-15], coalescence and breakup [16-20] and heat/mass transfer across the interface [21, 22]. A variety of numerical models suited for surface force dominated flows exist [23]. Common are continuum based methods like volume-of-fluid (VOF) [24], level set (LS) [25], phase-field (PF) [26] and front-tracking [27], mesoscopic methods like lattice Boltzmann (LB) [28] and particle based methods like smooth particle hydrodynamics (SPH) [29]. In this paper, we evaluate the accuracy of two continuum methods for gas-liquid microfluidic applications, namely the VOF and the PF method both implemented in OpenFOAM®.

Originally, VOF is a finite volume-based geometrical sharp-interface approach where the volume fraction α is introduced to discriminate the phases [24]. While interface cells contain both phases and thus have values in the range $0 < \alpha < 1$, single

phase cells have a value of $\alpha = 1$ or $\alpha = 0$. Geometrical VOF methods [24] explicitly reconstruct the interface of zero thickness by simple line interface calculation (SLIC) [30] or, nowadays, by variants of piecewise linear interface calculation (PLIC) [31-33]. The interface advection includes geometric information in the flux computation. This prevents interface thickening due to numerical diffusion, but leads to difficult, yet feasible incorporation in unstructured mesh approaches [34, 35]. Algebraic VOF methods solve an advection equation for α while the exact interface position and orientation remain veiled. To limit smearing by numerical diffusion, various interface-sharpening strategies have been proposed [36-38] providing confinement to a width of two to three mesh cells [39]. The main advantage of both VOF variants is their ability to secure mass conservation. A comparison of four VOF variants can be found in [40].

The phase-field method belongs to diffuse interface (DI) methods where the interface is not sharp but represented by a transition layer with small but finite thickness across which physical quantities vary smoothly but rapidly [41]. The thickness of the DI is several orders of magnitude larger than the physical interface thickness. Provided the DI model scales properly, such an artificially thickened interface can still represent the physical interfacial dynamics. PF methods use a smooth phase-field function denoted as order parameter to distinguish between the two phases. The interface evolution is modelled with the thermodynamically motivated Cahn-Hilliard [42] or Allen-Cahn equation [43]. A distinct advantage of PF methods is elegant modelling of topological changes (coalescence/breakup) with the drawback of potential apparent mass losses [44]. A review of PF methods for multi-component fluid flows is given in [45].

In this work, we focus on flows consisting of two immiscible incompressible Newtonian fluids and evaluate the algebraic VOF code `interFoam (IF)` [46] and

the PF code `phaseFieldFoam (PFF)` [47, 48], both implemented in the open

source software OpenFOAM®. In the evaluation of `IF` and `PFF` we especially focus on

so-called spurious or parasitic currents, artificial flows at the interface caused by

numerical inaccuracies [49, 50]. A prominent role on the formation of spurious currents

(SC) is played by inclusion of surface tension forces into the Navier-Stokes-equations.

Sharp interface (SI) methods commonly employ the continuum surface force (CSF)

model [51], which treats surface tension as a volume force density restricted to the

interface. State-of-the-art SI methods rely on balanced force implementations of the

CSF method. There, the surface tension and pressure gradient forces are discretised in

the same way and at exactly the same locations to ensure their balance on a discrete

level in order to supress SC in the absence of any flow [50, 52, 53]. Employing height

functions [50, 54] or other advanced methods for curvature calculation [55] reduces SC

for SI methods, while interface advection across the simulation domain leads to a

significant increase [56]. Popinet [57] reduced SC in static scenarios to machine

precision using PLIC-VOF with height functions and a balanced force CSF method. He

pointed out that well-balanced CSF implementations are not momentum conserving and

showed that SC still prevail for test cases with moving interfaces. He also notes that

what is interpreted as SC is sometimes an interfacial capillary wave stemming from the

deviation of the discretised interface shape from the equilibrium interface shape.

Improving the initialisation of the α field by advanced methods [55, 58] can reduce this

form of SC and result in more stable solutions [55]. Even today, none of the methods

presented in review [59] satisfies both well-balancing and momentum conservation.

In the PF model, capillary forces have first been incorporated into the Navier-

Stokes-equations by the pioneering model H of Hohenberg and Halperin [60] (valid for

matched phase densities). Phase-field inspired surface tension models assume a balance of the change in kinetic energy with the change in free energy. In contrast to the CSF approach that models surface tension *forces*, PF methods thus model fluid *energy* instead. A variational derivative of the free energy with respect to the order parameter C yields the chemical potential ϕ. Surface tension can then be modelled as $-C\nabla\phi$ which is the continuum surface tension forcing in its potential form [26]. Because of incompressibility, this potential form can also be written as $\phi\nabla C$ [26]. The potential formulation converges to the classical surface tension force as $\varepsilon \rightarrow 0$ [61] and is able to reduce SC by mesh refinement [62]. A different approach to account for surface tension in PF simulations is by incorporating the CSF model into the Navier-Stokes equations [63] instead using a potential formulation. He and Kasagi [64] performed PF simulations with both approaches and showed that a CSF model results in significant SC while a potential formulation drastically reduces SC. Lee and Kim [65] compared the performance of different CSF implementations in PS simulations and found for some first order convergence of SC with mesh refinement.

In summary, SC in CSF implementations mainly stem from an inconsistent discretisation and thus imbalance of surface tension and pressure gradient forces and from inaccurate curvature estimation compromising even balanced force discretisation. SC also arise in LB [66], SPH [67] and even in interface-fitted moving mesh methods [68], there however at very small magnitude. Independent of the method, the magnitude of SC increases with surface tension and density ratio. Due to the typically very low velocity of gas-liquid flows in microfluidic devices, the magnitude of SC may easily reach the order of the main flow thus severely disturbing the flow field.

Most literature studies on SC consider simplified conditions with similar or equal phase densities and viscosities [49, 51, 52, 56, 57, 63, 65, 69-74], entirely non-dimensional test cases [75], artificially large drops [50, 76, 77] or combinations of these restrictions. There are only very few studies, where the practically most relevant air water-system is considered for a droplet [78] or a bubble [64]. Furthermore, these studies are often restricted to a limited number of time steps. Here, we run simulations until steady or quasi-steady state, targeting on the emergence of SC in the practical relevant scenario of a submillimetre air bubble in water at static equilibrium, a test case prone to SC. Before that, we evaluate for comparison the performance of IF and PFF for two established SC test cases from literature with simplified conditions [70, 76]. The IF and PFF results for submillimetre air bubbles of different size in water are then evaluated with respect to interface thickness, bubble shape and displacement, mass conservation, interfacial pressure jump and SC.

The remainder of this paper is organised as follows. In Section 2, the mathematical framework together with details on the implementation of VOF and PF methods in OpenFOAM® are presented. Section 3 is devoted to the computational setup and evaluation procedure. Sections 4 and 5 present the results for the SC test cases from literature and the submillimetre air bubble in water, respectively. Finally, the paper provides conclusions in Section 6.

2   Mathematical framework and numerical methods

Flows of two isothermal, immiscible, incompressible Newtonian fluids are governed by the Navier-Stokes equation describing the momentum balance and the solenoidal condition representing the mass balance

$$\frac{\partial(\rho \mathbf{u})}{\partial t} + \nabla \cdot (\rho \mathbf{u}\mathbf{u}) = -\nabla p + \nabla \cdot \tau + \mathbf{f}_{\mathrm{b}} + \mathbf{f}_{\sigma} \quad \text{and} \quad \nabla \cdot \mathbf{u} = 0 \qquad (1)$$

with velocity field $\mathbf{u}$, time t, pressure p, and viscous stress tensor $\tau = \mu\left[(\nabla \mathbf{u}) + (\nabla \mathbf{u})^{\mathrm{T}}\right]$. The density ρ and dynamic viscosity μ vary locally depending on the phase distribution. Surface tension forces are represented by $\mathbf{f}_{\sigma}$. This work disregards gravity and other body forces so that $\mathbf{f}_{\mathrm{b}} = 0$.

2.1 Algebraic volume-of-fluid method

A widely used implementation of an algebraic VOF method in OpenFOAM® for two incompressible, isothermal immiscible fluids is `interFoam (IF)` [46], see also [69] for a good description of this code. In `IF`, the volume fraction α of one phase (here the continuous liquid phase) describes the phase distribution. `IF` essentially solves the equation

$$\frac{\partial \alpha}{\partial t} + \nabla \cdot (\alpha \mathbf{u}) = 0, \qquad (2)$$

albeit with some needed modifications to avoid the serious numerical diffusion issues. Being based on the concept of flux corrected transport [79], the solution procedure involves the Multidimensional Universal Limiter with Explicit Solution (MULES) to keep the VOF data bounded. In the interface region, a compressive velocity directed normal to the interface serves to limit numerical smearing. In the present simulations, the compressive factor is set to unity, see [69, 70] for details.

Density and viscosity in the Navier-Stokes equation are averaged arithmetically

$$\rho(\alpha) = \rho_{\mathrm{L}}\alpha + \rho_{\mathrm{G}}(1-\alpha), \quad \mu(\alpha) = \mu_{\mathrm{L}}\alpha + \mu_{\mathrm{G}}(1-\alpha), \qquad (3)$$

where the indices L and G stand for liquid and gas, respectively. The surface tension force is implemented through the CSF model as $\mathbf{f}_{\sigma} = \delta\sigma\kappa\mathbf{n} = \sigma\kappa\nabla\alpha$. The interface curvature is given by $\kappa = \nabla \cdot (-\mathbf{n})$ where the unit normal vector $\mathbf{n} = \nabla\alpha/|\nabla\alpha|$ is computed using the updated α values obtained from solution of Eq. (2). The pressure-

8

velocity coupling is performed by the PIMPLE algorithm, a combination of the PISO (pressure-implicit with splitting of operators) algorithm [80] and SIMPLE (semi-implicit method for the pressure linked equations) algorithm [81].

For discretisation, second order schemes are adopted as follows. The discretisation of gradient operators (`gradSchemes`) and Laplace operators (`laplacianSchemes`) is performed with the Gauss linear and Gauss linear uncorrected schemes, respectively. For divergence operators (`divSchemes`), the Gauss vanLeer and Gamma interfaceCompression schemes are used for the momentum and volume fraction equations, respectively. For discretisation of the time derivatives (`ddtSchemes`), the Crank-Nicholson scheme is chosen.

In the present paper, the widely used standard `IF` solver is employed (foam-extend-3.1). No special measures haven been undertaken to reduce spurious currents. For techniques to reduce SC in `IF`, the interested reader is referred to [55, 74, 82-85].

2.2   *Phase-field method*

Phase-field methods rely on a dimensionless order parameter, the phase field, which varies continuously over the thin interfacial layer and is mostly uniform in the bulk phases. Here, the order parameter takes the value $C = 1$ in the liquid bulk and $C = -1$ in the gas bulk while values in the range $-1 < C < 1$ correspond to the diffuse interface.

The phase evolution is described by the convective Cahn-Hilliard equation

$$\frac{\partial C}{\partial t} + (\mathbf{u} \cdot \nabla)C = M\nabla^2\phi, \tag{4}$$

where M is the Cahn-Hilliard mobility (diffusion parameter). The chemical potential

$$\phi = \frac{\lambda}{\varepsilon^2}(C^3 - C) - \lambda\nabla^2 C \tag{5}$$

represents the change rate of free energy with respect to C and consists of a bulk and

interface contribution. Here, λ is the mixing energy density and ε the capillary width.

For stagnant fluids and at steady state, the right hand side of Eq. (4) is zero. In one-dimension, the corresponding equilibrium profile across a planar interface is

$$C = \tanh\left(\frac{x}{\sqrt{2}\varepsilon}\right),\tag{6}$$

where x is the direction normal to the interface. Fig. 1 shows the profile from Eq. (6) for a capillary width of $\varepsilon = 10\,\mu\text{m}$. In the region with $-0.9 < C < 0.9$, the equilibrium profile changes rapidly but smoothly. The width $L_{C,\text{planar}} = 2\sqrt{2}\varepsilon\tanh^{-1}(0.9) = 4.164\varepsilon$ of this region often serves as a measure for the thickness of the DI. A useful non-dimensional quantity to characterise the interface thickness is the Cahn number which relates the capillary width to a macroscopic length scale, here the initial bubble diameter so that $Cn := \varepsilon / D_0$.

From Eq. (6), the surface tension, which is by definition the excess energy present in the system due to the presence of the interface, can be found to be [26, 86]

$$\sigma = \int_{-\infty}^{\infty} \lambda\left(\frac{dC}{dx}\right)^2 dx = \frac{2\sqrt{2}}{3}\frac{\lambda}{\varepsilon}\tag{7}$$

For the present simulations, σ and ε serve as input parameters so that λ follows from Eq. (7). Interface curvature changes phase-field surface tension. The induced error in both surface tension and pressure jump is a quadratic function of interface thickness times curvature, the coefficient of this error being small [26].
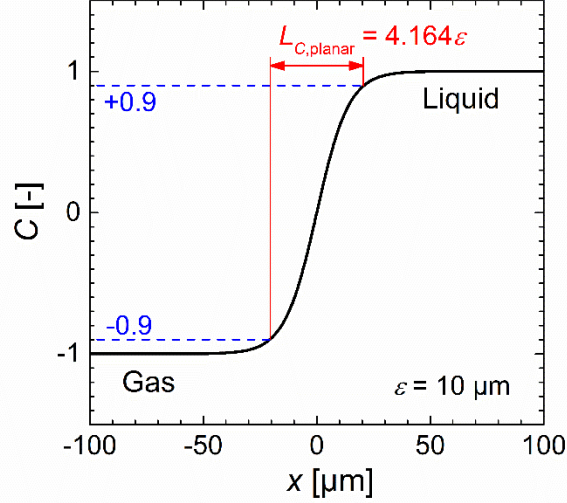
Fig. 1. Profile of the order parameter across a planar diffuse interface in equilibrium.

Equations (4) and (5) are coupled with the Navier-Stokes equations (1). There, density and viscosity depend on the order parameter, similar to Eq. (3) in `IF`, as

$$\rho(C) = \frac{1}{2}\,\rho_{L}(1+C) + \rho_{G}(1-C)\,, \quad \mu(C) = \frac{1}{2}\,\mu_{L}(1+C) + \mu_{G}(1-C)\,, \quad (8)$$

Following [26, 87], the surface tension force is incorporated by $\mathbf{f}_{\sigma} = -C\nabla\phi$.

The coupled Cahn-Hilliard Navier-Stokes equations are solved by the code `phaseFieldFoam` (`PFF`) in a segregated manner using OpenFOAM-1.6-ext. [47, 48, 88]. The discretisation schemes in `PFF` are similar to those in `IF` listed above, with exception of the divergence operator (Gauss Gamma 0.5). The solution procedure from time step $n \triangleq t^{n}$ to $n+1 \triangleq t^{n+1}$ is as follows:

1) Compute ϕ^{n} using Eq. (5).

2) Solve Cahn-Hilliard Eq. (4) for C^{n+1} using ϕ^{n} and $\mathbf{u}^{n}$.

3) Use C^{n+1} to determine ρ^{n+1} and μ^{n+1} by Eq. (8), ϕ^{n+1} by Eq. (5) and
   $\mathbf{f}_{\sigma}^{n+1} = -C^{n+1}\nabla\phi^{n+1}$.

11

4) Solve Navier-Stokes Eqs. (1) for $\mathbf{u}^{n+1}$ and p^{n+1} with the PISO iteration algorithm using ρ^{n+1}, μ^{n+1} and $\mathbf{f}_\sigma^{n+1}$.

3   Numerical setup and evaluation procedure

The test case of a static circular bubble is chosen due to its simplicity and informative value. Because the system is in mechanical equilibrium, any terminal deviation from (i) the circular shape, (ii) the Laplace pressure jump and (iii) the static velocity field can be attributed to numerical inaccuracy. This section describes the setup for a static circular submillimetre air bubble in water in absence of gravity, the results of which are presented in Section 5. The setup for both SC test cases from literature is similar and any difference is mentioned in Section 4, where the corresponding results are discussed.

3.1   *Computational setup and fluid properties for air bubble in water*

All simulations are two-dimensional, transient and employ a Cartesian co-ordinate system in a square computational domain. The initial conditions consist of a circular bubble in the centre of the domain surrounded by an immiscible outer phase. Both phases are initially at rest. The initial bubble diameter is D_0 and the co-ordinates of the initial bubble centre are $\mathbf{x}_0 = (x_0, y_0)^{\mathrm{T}} = (0,0)^{\mathrm{T}}$. In all simulations the domain size is $L_x = L_y = 2D_0$, discretised by uniform square mesh cells of size $\Delta x = \Delta y = h$. In the sequel, we refer to the spatial resolution by the number of cells per initial diameter $N_D := D_0 / h$. The grid thus consists of $N_x = N_y = 2N_D$ mesh cells in each direction and $N_\Omega = 4N_D^2$ mesh cells in the entire domain. In one dimension and at equilibrium, the width of the diffuse interface in the PF method is $L_{C,\mathrm{planar}} \approx 4\varepsilon$. The number of grid cells used for resolving the diffuse interface is $N_C := 4\varepsilon / h = 4CnN_D$. Previous simulations showed that for obtaining accurate results with PFF values of N_C larger

12

than about $4-6$ are required [47, 88-90]. At the sides of the computational domain, periodic boundary conditions are used. Thus, no symmetry conditions are assumed that could supress any artificial displacement of the bubble from its initial position. The physical properties of the gas and liquid phases correspond to air and water and are as follows: $\rho_G = 1.2\,\text{kg/m}^3$, $\mu_G = 1.837 \times 10^{-5}\,\text{Pa} \cdot \text{s}$, $\rho_L = 997\,\text{kg/m}^3$, $\mu_L = 9.97 \times 10^{-4}\,\text{Pa} \cdot \text{s}$, $\sigma = 0.07286\,\text{N/m}$.

3.2 *Initialisation of discrete phase distribution*

The numerical simulations require specifying the discrete initial phase distribution. In order to ensure consistency of the initial data with the underlying mathematical approach, the procedure differs for `IF` and `PFF` and reflects the VOF method being a sharp interface method in contrast to the PF method being a diffuse interface method.

In `IF`, the dictionary `setFieldsDict` initialises the discrete field $\alpha(\mathbf{x})$ by filling mesh cells initially either completely with gas or with liquid corresponding to a SLIC-like interface representation [30]. This initialisation results in a deviation of the discrete initial bubble area $A_{0,\text{dis}}$ from the nominal initial area $A_0 = \pi D_0^2 / 4$. The relative deviation $(A_{0,\text{dis}} - A_0) / A_0$ decreases with resolution and is $-1.4, 0.64, -0.31, 0.08$ percent for $N_D = 25, 50, 75, 100$. Similarly, the effective discrete initial bubble diameter $D_{0,\text{dis}} = \sqrt{4 A_{0,\text{dis}} / \pi}$ deviates from D_0. The diameter deviates about half as much as the area with values below 0.7% for all cases.

Contrary to the sharp interface in `IF`, the discrete initial order parameter field in `PFF` represents a diffuse interface. For that purpose, the planar equilibrium profile of Eq. (6) is adapted for a circular bubble

$$C(\mathbf{x}) = \tanh\left(\frac{\sqrt{(x - x_0)^2 + (y - y_0)^2} - 0.5 D_0}{\sqrt{2}\varepsilon} \right). \tag{9}$$

The relative deviations $(A_{0,\text{dis}} - A_0)/A_0$ and $(D_{0,\text{dis}} - D_0)/D_0$ are, for an identical value of N_D, in PFF about ten times smaller than in IF.

The chosen initialisations for the phase distribution mean that neither in IF nor in PFF the systems is initially in complete mechanical equilibrium. Accordingly, the prompt velocity field forming when starting a simulation from both phases at rest is not necessarily spurious. In the course of the simulation, however, the phase distribution is expected to develop towards a steady state representing mechanical equilibrium where then any remaining finite velocity magnitude has to be considered spurious.

3.3 Time step control

Transient numerical simulations require an appropriate time step width Δt. Important in this context is the Courant number $Co = U_{\max}\Delta t / h$ where $U_{\max}(t)$ is the magnitude of the maximum velocity in the computational domain. Roenby et al. [34] noted that from their experience the explicit MULES scheme in IF is limited to $Co \leq 0.1$ if accuracy is important. In the present study we therefore restrict the maximum time step to $\Delta t_{Co_{\max}} = Co_{\max} h / U_{\max}$ where $Co_{\max} = 0.1$. Thus, for small values of $U_{\max}$ the time step increases thereby reducing the computational costs. To avoid excessively large time steps that arise in the limit of vanishing SC, i.e. $U_{\max} \to 0$, an upper limit $\Delta t_{\max} = 5\,\mu\text{s}$ is specified empirically so that the variable time step width is

$$\Delta t = \min(\Delta t_{Co_{\max}}, \Delta t_{\max}). \tag{10}$$

When introducing their CSF model, Brackbill et al. [51] gave the time step criterion in Eq. (11) to ensure stability with respect to propagating capillary waves along the interface in case of explicit treatment of surface tension

$$\Delta t_{\text{BKZ}} \leq \sqrt{\frac{(\rho_{\text{L}} + \rho_{\text{G}})h^3}{4\pi\sigma}}. \tag{11}$$

14

In practice, such capillary waves are damped by viscous and inertial forces. To account for the enhanced stability due to these effects, Galusinski and Vigneaux [91] proposed a less stringent extended time step criterion which includes two code-dependent constants. Deshpande et al. [69] studied spurious currents in IF for a 2D droplet with diameter $D_0 = 500\,\mu m$ under the restriction of matched density and viscosity of the phases to determine these constants for that code. From 80 simulations with varying combinations of density and viscosity, they derived the time step criterion in Eq. (12) to limit the growth of SC and ensure that the drop position is stable

$$\Delta t_{\mathrm{DAT}} \leq \frac{1}{2}\left\{10\frac{\mu h}{\sigma} + \sqrt{\left(10\frac{\mu h}{\sigma}\right)^2 + 0.04\frac{\rho h^3}{\sigma}}\right\}. \tag{12}$$

For an air bubble in water it is unclear, which density and viscosity should be used in this criterion. For $h = 6.6\,\mu m$ (corresponding to $D_0 = 500\,\mu m$ and $N_D = 75$), Eq. (12) yields $\Delta t_{\mathrm{DAT}} = 0.95\,\mu s$ and $\Delta t_{\mathrm{DAT}} = 0.019\,\mu s$, when density and viscosity of water and air are used, respectively. The latter time step is too small to allow for a comprehensive simulation study. Therefore, the criterion of Eq. (12) is used in two simulations only to check whether it applies for non-matched phase properties as well, which will be shown not to be the case.

For the PF method, Aland [92] found by numerical tests using a Crank-Nicolson scheme and equal densities in both phases the empirical time step restriction

$$\Delta t_{\mathrm{Aland}} < 7\varepsilon\rho^{2/3}M^{1/3}\sigma^{-1/3}. \tag{13}$$

This criterion is independent of the grid size and very different from Eqs. (11) and (12). We evaluated Eq. (13) using the liquid density for the test cases in Table 1. The maximum time step is in the range $1.1-11.4\,\mu s$ which is of same order of magnitude as $\Delta t_{\mathrm{max}} = 5\,\mu s$.

3.4   Test cases

For a submillimetre air bubble in water, four different bubble diameters are considered, namely 250, 500, 750 and 1000 µm. Among these, the initial bubble diameter $D_0 = 500\,\mu\text{m}$ serves as base case. Simulations are performed for parameters as listed in Table 1. In IF, the number of mesh cells per bubble diameter (N_D) is the sole free parameter. A variation of N_D results in a variation of h and may – as discussed in the previous subsection – also result in a variation of Δt .

In PFF, two further independent numerical parameters are varied besides N_D . The first one is the capillary width ε , respectively the Cahn number Cn . The number of mesh cells per interface width $N_C = 4 Cn N_D$ varies with the two former parameters. The second independent parameter is the mobility M. Jacqmin [26] suggested the scaling $M \propto \varepsilon^2$ and we set $M = \chi \varepsilon^2$ with a constant χ , mostly of value $\chi = 0.1\,\text{m}\cdot\text{s/kg}$. To study the effect of mobility, we compared for one test case simulation results obtained with $\chi = 0.1\,\text{m}\cdot\text{s/kg}$ and $\chi = 1\,\text{m}\cdot\text{s/kg}$ while all other parameters including Δt are fixed. It turned out that the value of χ slightly effects the time history of SC but is without influence on the terminal value. This is plausible, since M appears on the right-hand-side of Eq. (4), representing a diffusion coefficient which affects the order parameter field only when the system it is out of equilibrium. In equilibrium, the chemical potential ϕ is uniform so that the diffusion term with prefactor M vanishes.

Table 1 Overview on test cases and numerical parameters for a submillimetre air bubble in water with fluid properties as given in Section 3.1. For `IF`, N_D is the only numerical parameter. The test case with $N_D = 25$ is only computed with `IF` and that with $N_D = 200$ only with `PFF`. The results for these test cases are presented in Section 5.

Parameters `IF`/`PFF`		Additional parameters in `PFF`			
D_0 [μm]	N_D [−]	ε [μm]	Cn [−]	N_C [−]	χ [m·s/kg]
250	100	5	0.02	8	0.1
500	25				
	50	10	0.02	4	0.1
		20	0.04	8	0.1
		20	0.04	8	0.00625
	75	10	0.02	6	0.1
	100	10	0.02	8	0.1
		10	0.02	8	0.025
	200	5	0.01	8	0.1
750	100	15	0.02	8	0.1
1000	100	20	0.02	8	0.1

3.5 *Evaluation procedure and quantification of errors*

3.5.1 *Spurious currents*

Since both phases are stagnant and the system is by definition in mechanical equilibrium, all observed velocities are spurious in the end. Therefore, the maximum spurious currents magnitude is the maximum velocity in the computational domain

$$U_{\text{sc}} = U_{\text{max}} = \max_{i,j} \left\| \mathbf{u}_{i,j} \right\| , \qquad (14)$$

where the subscripts i and j denote the cell indices of the structured Cartesian mesh. The velocity $U_{sc}(t)$ is determined for each time step of the transient simulation.

3.5.2   Bubble displacement and mean bubble diameter

In order to determine the bubble displacement, the bubble barycentre is computed

$$\mathbf{x}_{bc} = \frac{\sum_{i,j} \gamma_{i,j} \mathbf{x}_{i,j}}{\sum_{i,j} \gamma_{i,j}}, \qquad (15)$$

where $\mathbf{x}_{i,j}$ denotes the location of the mesh cell centre and the summation is over all cells. In Eq. (15), γ is a master field for the gas volume fraction. For IF, it is $\gamma = 1 - \alpha$ while for PFF it is $\gamma = (1 - C)/2$. The bubble displacement is $x_{B} := \|\mathbf{x}_{bc} - \mathbf{x}_{0}\|$. Deshpande et al. [69] classified simulations with different Δt as stable ($x_{B} \leq h$) and unstable ($x_{B} > h$), cf. Eq. (12). Since simulations with $x_{B} > h$ may yield converged solutions as well, we denote the criterion here as position-stable/position-unstable.

Throughout the paper, we use the isoline $\gamma = 0.5$ to determine the interface position and to discriminate between the phases. For all mesh cells cut by this isoline, the distance from the bubble centre is determined. Averaging of all values and multiplying by two yields the mean bubble diameter D_{m}. Furthermore, its standard deviation s_{D} quantifies the bubble circularity. We remark that determining isolines (either in OpenFOAM® directly or in a post-processing step with ParaView®) involves interpolation and thus introduces an interpolation error, which is hard to quantify.

3.5.3   Interface thickness

For PFF, the relation between the diffuse interface thickness and the input parameter ε is of interest, since for a circular interface no analytical equilibrium solution exists, such as Eq. (6) for the planar case. For IF simulations, the relation between the interface thickness and the mesh size is of interest for evaluating the performance of the interface

18

compression scheme. Approaching the physical interface thickness by continuously reducing numerical interface thickness should in principle lead to more realistic results in both methods. However, thinner interfaces yield steeper density and viscosity gradients, amplifying SC.

To quantify the interface thickness (δ_{int}), we use two isolines. In `IF`, δ_{int} is computed as the distance between the inner isoline $\alpha = 0.1$ and the outer isoline $\alpha = 0.9$. In a similar manner, δ_{int} is determined in `PFF` using $C = -0.9$ and 0.9. In this way, δ_{int} is evaluated from the profiles of α and C along the horizontal and vertical midplane of the computational domain. This yields four values of δ_{int} at different positions, which are averaged arithmetically.

3.5.4 Laplace pressure jump

To evaluate the accuracy of the simulations with respect to the pressure field, we compare the numerical pressure jump with the Young-Laplace pressure $\Delta p_{\text{exact}} = 2\sigma / D_0$. The average numerical pressure in both phases is determined by a threshold based procedure similar to [50, 70] which ignores the pressure in the interface region. Hence, $p_{\text{G,partial}}$ and $p_{\text{L,partial}}$ are the averaged values of the pressure inside ($\gamma \geq 0.99$) and outside ($\gamma \leq 0.01$) the bubble, respectively. These threshold values are somewhat arbitrary and differ from the values 0.95 und 0.05 used in [70]. In the present case, the averaged pressure inside the gas bubble thus includes regions further from the interface. The numerical pressure jump is given by $\Delta p_{\text{num}} = p_{\text{G,partial}} - p_{\text{L,partial}}$.

4   Results for spurious currents test cases from literature

Before presenting simulation results for a submillimetre air bubble in water in Section 5, we compute with `IF` and `PFF` two less demanding test cases on spurious currents for

comparison with literature. Matched densities and viscosities of both phases eliminate the influences of density and viscosity contrasts [70]. Using inviscid phases considers the density contrast and quantifies the spurious currents after a single time step [76].

4.1 Matched densities and viscosities

Popinet and Zaleski [93] considered test cases with matched density and viscosity with a front-tracking method and found a linear proportionality $U_{sc} \propto \sigma / \mu$ over a wide range of Ohnesorge numbers $(Oh := \mu / \sqrt{\sigma \rho D_0})$. For a fixed value of Oh, the capillary number $Ca_{sc} := U_{sc} \mu / \sigma$ is thus about constant and independent on grid size. Albadawi et al. [70] computed a test case with IF (OpenFOAM® 2.0) for $D_0 = 10 \, \text{mm}$, $\rho_L / \rho_G = 1$, $\mu_L / \mu_G = 1$ and $Oh^{-2} = 1000$. They considered a domain of size $L_x = L_y = 5 D_0$ and varied the grid resolution in the range $10 \leq N_D \leq 100$. The time step was $\Delta t = h / (10 \, \text{m s}^{-1})$ and the simulations were run until $t = 0.1 \, \text{s}$. In accordance to [93], Ca_{sc} stayed constant around 0.002 and no convergence with grid refinement was obtained, meaning a decrease of U_{sc} with decrease of h.

In this work, we reconsider the test case of Albadawi et al. [70] with equal domain size, time step and Ohnesorge number using $D_0 = 10 \, \text{mm}$, $\rho_L = \rho_G = 1000 \, \text{kg/m}^3$, $\mu_L = \mu_G = 0.001 \, \text{Pa} \cdot \text{s}$ and $\sigma = 0.01 \, \text{N/m}$. The grid resolution N_D is varied between 10–100 in IF and 50–100 in PFF, the latter translating to an interface resolution with $4 \leq N_C \leq 8$ mesh cells at constant capillary width. While the simulations in [70] are ran until $t = 0.1 \, \text{s}$, our final time is $t = 10 \, \text{s}$ because the SC did not reach a terminal value for $t = 0.1 \, \text{s}$. For $t = 10 \, \text{s}$, U_{sc} reached in all PFF simulations a constant value, whereas in some IF simulations U_{sc} is still slightly changing in time. All simulations are position-stable with $x_B / h < 0.012$ in IF and $x_B / h < 2 \cdot 10^{-8}$ in PFF. Fig. 2 shows the IF and PFF results for Ca_{sc} at $t = 0.1 \, \text{s}$ and $t = 10 \, \text{s}$ versus grid resolution (with N_D

displayed at the bottom and h at the top x-axis). Included for comparison are the IF results from [70] for $t = 0.1\,\text{s}$. Since Fig. 2 contains a lot of information, we discuss the results of both codes separately beginning with IF.

For $t = 0.1\,\text{s}$, the present IF results are very close to those in [70]. For $t = 10\,\text{s}$, the SC are reduced by a factor $3 - 40$ as compared to $t = 0.1\,\text{s}$. The values of Ca_{sc} at both instants in time are almost independent on mesh resolution. This behaviour can be explained by the implementation of the CSF model in IF. Convergence of SC with grid refinement in the CSF model can only be achieved if the curvature estimation converges with mesh refinement and if at the same time the discrete force balance between pressure gradient and surface tension is ensured by a consistent (balanced) implementation. Deshpande et al. [69] evaluated the performance of IF and found that the implementation of pressure gradient and surface tension term seems to be consistent and reaches the necessary discrete force balance. As mentioned in Section 2.1, in IF interface curvature is calculated from the original (i.e. unsmoothed) α field. Approaches that are more sophisticated employ some pre-processing of the discontinuous volume fraction field, in order to get a smoother field that can be used to achieve more accurate curvature estimations. Common approaches are convolution techniques for the α field or the usage of height functions. While smoothing techniques can reduce SC by several orders of magnitude [94], reaching a convergent behaviour with grid refinement has proven to be a significantly more challenging task.

For PFF, Fig. 2 shows that the values of Ca_{sc} at both instants in time are much smaller as compared to IF. For $t = 10\,\text{s}$, the SC in PFF are reduced by a factor $40 - 60$ as compared to $t = 0.1\,\text{s}$. In contrast to IF, the PFF results show an almost second-

21

order convergence for Ca_{sc} so that finer meshes result in lower SC. The reasons for these behaviours will be discussed in Section 4.3.
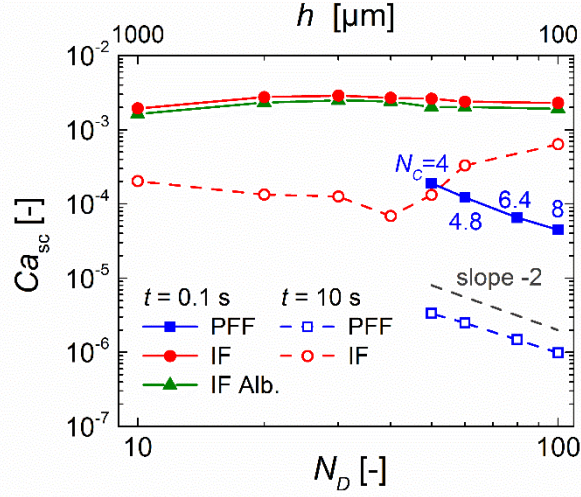

Fig. 2. Influence of mesh resolution on Ca_{sc} for matched density and viscosity ($D_0 = 10\,\text{mm}$, $Oh^{-2} = 1000$). Comparison of IF and PFF ($Cn = 0.02$, $\varepsilon = 0.2\,\text{mm}$, $N_C = 4CnN_D$, $\chi = 0.1\,\text{m}\cdot\text{s/kg}$) results at two instants in time with results from [70] (IF Alb.).

4.2 Inviscid phases

Yokoi used a CLSVOF method and simulated a 2D drop with diameter $D_0 = 2\,\text{m}$ in a domain $L_x = L_y = 2D_0$ on a Cartesian grid [76]. Surface tension is modelled by four different CSF approaches (balanced/unbalanced with/without density scaling). Due to momentum conservation, small momentum errors near the interface of a high-density phase transfer to high velocities in the low-density phase. Density scaling shifts the smoothed interface delta function towards the higher density phase and reduces SC [50, 76]. To study the convergence with respect to SC, Yokoi performed simulations with different grid resolution for a single time step ($\Delta t = 1\,\mu\text{s}$). Both phases are inviscid with

densities $\rho_L = 1\,\text{kg/m}^3$ and $\rho_G = 0.001\,\text{kg/m}^3$ and surface tension $\sigma = 1\,\text{N/m}$.

In this subsection, Yokoi's inviscid test case is repeated with `IF` and `PFF` using kinematic viscosities $\mu_L / \rho_L = \mu_G / \rho_G = 10^{-40}\,\text{m}^2/\text{s}$. In contrast to Section 4.1, quantifying SC by the capillary number Ca_{sc} is not meaningful for an inviscid test case so that the results are presented in terms of U_{sc} instead. Fig. 3 (a) compares the SC in `IF` with Yokoi's results for the two unbalanced methods where N_D is in the range 10−640. The SC in `IF` are about three orders of magnitude larger than in Yokoi's standard CSF method. In all three methods, the SC increase as h decreases (and N_D increases). Thus, the results deteriorate with grid refinement. This divergence is caused by the imbalance between surface tension and pressure gradient forces resulting from different discrete approximations for $\nabla\alpha$ in the CSF model and ∇p. For finer grids, the gradients become steeper and the discrepancy increases, so SC increase.

Fig. 3 (b) compares the results of Yokoi's two balanced methods with those of `PFF`. As mentioned before, `PFF` requires $N_C \geq 4$ to ensure an adequate resolution of the diffuse interface corresponding to $N_D \geq Cn^{-1} = 50$ for $Cn = 0.02$ as used here. For Yokoi's methods, the SC are about 2-3 orders of magnitude smaller than in `PFF`. For all three methods, the SC decrease as h decreases. For small values of N_D, Yokoi's methods shows a second order convergence which changes into a first order one for larger values of N_D, while the `PFF` results show a second order convergence similar to the previous test case.
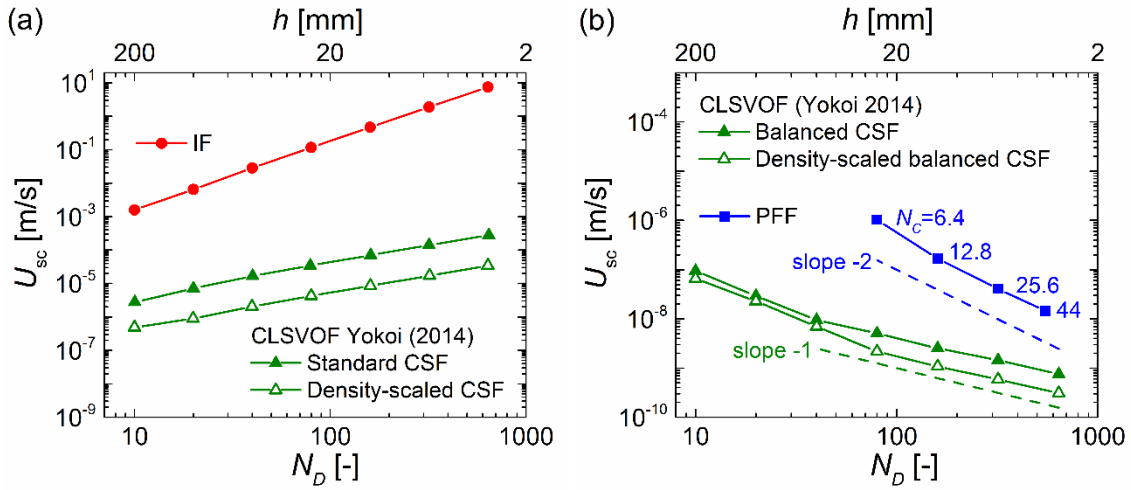
Fig. 3. Influence of mesh resolution on spurious currents after one time step for an inviscid drop with diameter $D_0 = 2\,\text{m}$. (a) Comparison of `IF` results with CLSVOF results of Yokoi [76] using unbalanced CSF models. (b) Comparison of `PFF` results ($Cn = 0.02$, $\varepsilon = 40\,\text{mm}$, $N_C = 4CnN_D$, $\chi = 0.1\,\text{m}\cdot\text{s/kg}$) with CLSVOF results using balanced CSF models [76].

At first glance, the results of Yokoi seem to indicate that convergence of spurious currents with grid refinement with a CSF model can be reached by simply assuring a balanced force implementation, disregarding any special treatment in curvature estimation. It should be noted, however, that the smooth level-set function was used for curvature calculation instead of the discontinuous volume fraction field. Additionally, an interpolation of curvature values for cell faces by solving a curvature advection equation was introduced. Furthermore, the convergence behaviour was investigated after a single time step, which might have erased the effects of inaccurate curvature estimation developing over time.

4.3   Discussion

The second order convergence of SC obtained with `PFF` for both test cases is remarkable, as no special measures for reducing SC have been undertaken and deserves a discussion.

In the chemical potential formulation surface tension is modelled as an energy associated with the gradient of the order parameter, cf. Eq. (7). Accordingly, the interfacial *energy* is "stored" in the diffuse interface region of the order parameter field and even persists for a *flat* interface. This is in contrast to the CSF approach, where surface tension *forces* arise only for *curved* interfaces. While accurate computation of interface curvature and its convergence with grid refinement is thus of paramount importance for convergence of SC in the CSF model, curvature computation is completely absent in the PF method. In `IF` and in SI methods in general, the thickness of the numerical interface is intimately related to h (cf. Section 5.2.1) which makes achieving convergence of curvature computation and SC a formidable task.

The behaviour with grid refinement of different curvature estimation approaches for a geometrical PLIC-VOF method was studied by Cummins et al. [54]. While their convolution technique gave no convergence, their height functions method showed second order convergence. Following this result, Francois et al. [50] showed that in their balanced force PLIC-VOF implementation second order convergence of SC with mesh refinement can be achieved with height functions while no convergence was reached with a convolution technique. Gerlach et al. [95] studied the behaviour of two geometric VOF approaches from literature [52, 96] and that of a coupled level-set VOF (CLSVOF) method, where the curvature is calculated from the smooth level-set function. None of these methods showed convergence of SC with mesh refinement.

Recently, Abadie et al. [56] showed that even an algebraic FCT-VOF code can reach second order convergence by making use of height functions in its curvature calculation. This is especially interesting since `IF` is also a FCT-VOF code and might show the same behaviour if a height function based curvature estimation is used, as done by Binz et al. [84]. Using the ordinary implementation without the extra effort in curvature calculation, both Deshpande et al. [69] and Albadawi et al. [70] reported a convergence of the curvature towards a systematically deviating value from the analytic solution, which is the reason for the behaviour of `IF` observed in Fig. 2.

In the PF method, the thickness of the diffuse interface is controlled by the capillary width ε, independent from mesh resolution. For a fixed value of the capillary width (respectively Cahn number), the smoothness of $C(\mathbf{x})$ and that of $\phi(\mathbf{x})$ as well thus increases with mesh refinement leading to a more accurate numerical representation of surface tension, cf. Eq. (7). The surface tension model used in `PFF` reads $\mathbf{f}_\sigma = -C\nabla\phi$ so that in the absence of any other forces, the balance between pressure gradient and surface tension becomes $\nabla p = -C\nabla\phi$. Consistent discretisation of the two gradient operators in OpenFOAM® (by using the same `gradSchemes` as done here) can thus result automatically in a balanced discretisation scheme.

In conclusion, the second order convergence of SC with mesh refinement can be attributed to three features of the PF method with free energy surface tension model: absence of curvature computation, modelling of interface thickness independent from mesh resolution and easy to achieve balanced discretisation. This second order convergence indicates that adaptive mesh refinement in the DI region can effectively alleviate SC.

5   Results for a submillimetre air bubble in water

In this section, we present the simulation results for the test cases described in Section 3 and listed in Table 1 considering a quiescent submillimetre air bubble in stagnant water. We first discuss the temporal evolution of the transient simulations and then focus on terminal results concerning phase distribution, pressure field and velocity field.

5.1   Temporal evolution

The temporal evolution of the simulations is evaluated by means of the time histories of the spurious currents $U_{sc}(t)$ and the bubble displacement $x_B(t)$. A steady state is assumed when both quantities are constant in time. Most PFF simulations reach a steady state until $t = 0.4\,\text{s}$. In some PFF simulations, x_B is constant while U_{sc} still slightly changes in time. All PFF simulations are position-stable ($x_B < h$). The IF simulations also reach a state when U_{sc} is either approximately constant in time or slightly oscillating around a time-independent mean value. However, this state does not always go along with a steady bubble position. Whether a simulation reaches a steady bubble position in IF depends on Δt. For the time step criterion in Eq. (10) with $\Delta t_{max} = 5\,\mu\text{s}$ a steady bubble position is obtained. However, the corresponding bubble displacement is often quite large and the bubble is not position-stable. To test, if the bubble displacement can be reduced by reducing the time step size, two additional simulations have been performed for $D_0 = 500\,\mu\text{m}$ with $N_D = 75$. The time steps $\Delta t_{max} = 0.8\,\mu\text{s}$ and $0.01\,\mu\text{s}$ meet the criterion of Eq. (12) when the density and viscosity of water and of air are used, respectively (cf. Section 3.3). The time step criterion from Eq. (11) gives $\Delta t_{BKZ} \leq 0.57\,\mu\text{s}$, a value in-between. Notably it turned out that neither the simulation with $\Delta t_{max} = 0.8\,\mu\text{s}$ nor that with $\Delta t_{max} = 0.01\,\mu\text{s}$ yields a steady bubble position but both result in a continued movement of the bubble through the periodic

domain. Obviously, the criterion in Eq. (12) derived empirically for matched densities and viscosities is not applicable to the present much more demanding test case of submillimetre air bubbles in water with large density contrast. The issue of the time step criterion for `IF` is not investigated further here and in the sequel only `IF` simulations with $\Delta t_{\max} = 5\,\mu s$ yielding a steady bubble position are considered for further analysis.

Fig. 4 (a) displays the velocity field for the `PFF` case with $D_0 = 500\,\mu m$ and $N_D = 75$ at $t = 0.4\,s$. Also shown are the interface position (black line) and the area between the isolines serving for determining the interface thickness (shaded in grey). The bubble shape is close to circular and steady in time. The velocity field due to spurious currents is symmetric with respect to the horizontal and the vertical midplane and the largest SC are directed tangential to the interface. The velocity fields and bubble shapes in the `PFF` simulations with $N_D = 50$ and $N_D = 100$ (not shown) are similar.

Fig. 4 (b) shows a similar visualisation of the velocity field for the `IF` case with resolution $N_D = 25$ at $t = 0.4\,s$. The bubble shape is close to circular and steady in time. The velocity field is symmetric with respect to the horizontal and vertical midplane with the largest SC pointing normal to the interface into the bubble. For the `IF` simulations with finer resolution displayed in Fig. 4c-h, the bubble centre has reached a steady position at $t = 0.4\,s$ as well. However, the bubble centre is more or less displaced from its initial position and the bubble shape is not steady but oscillating in time. For the case with $N_D = 50$, the bubble shape changes periodically between an elongate and prolate ellipse (Fig. 4 c, d). The same behaviour is observed for resolution $N_D = 75$ (Fig. 4 e, f). The bubble displacement and oscillation frequency are, however, increased as compared to $N_D = 50$. For $N_D = 100$, the bubble oscillates in a different

mode showing not two but four bulges (Fig. 4 g, h), with again increased frequency as compared to the case with $N_{\mathrm{D}} = 75$.

The IF shape oscillations in Fig. 4 c-h) are unphysical in the sense that the deformations are far bigger than the inaccuracies of the imperfect shape initialisation. As the inaccuracy of the shape initialisation decreases with mesh refinement, one may expect a decrease in displacement and oscillation amplitude for finer meshes. However, this is not the case; instead, the shape complexity and oscillation frequency increase with mesh resolution. Since there is no physical mechanism driving bubble displacement and shape oscillations, both are numerical artefacts. They arise because in IF the SC velocity field becomes asymmetric for $N_D \geq 50$. SC arise as local numerical artefacts and there is no reason for assuming that the corresponding velocity field stays fully symmetric during a simulation, especially if the degree of freedom (which increases with N_D) is sufficiently large. The above results indicate that in the present computations with the standard IF solver unavoidable local finite asymmetries of SC amplify for $N_D \geq 50$, resulting in bubble displacement and shape oscillations. While the shape oscillations may reflect natural (i.e. physical) vibration modes, the mechanism causing and driving them is not physical but purely numerical. In the sequel, shape oscillations will be disregarded from further analysis and all simulation results are evaluated for $t = 0.4\,\mathrm{s}$.
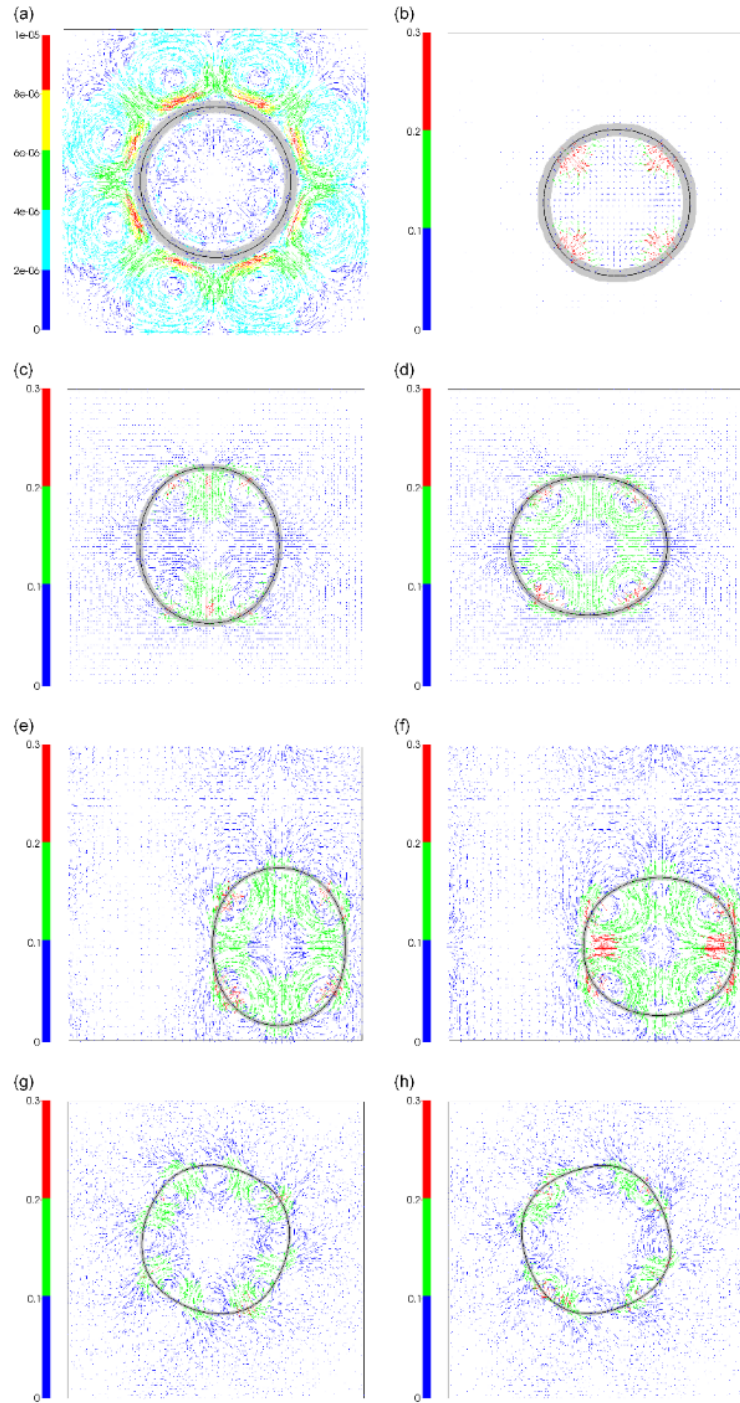
Fig. 4. Velocity field (arrows coloured with velocity magnitude in m/s) and bubble shape (black line) for $D_0 = 500 \, \mu\text{m}$. (a) PFF $N_\text{D} = 75$, $t = 0.4 \, \text{s}$; (b) IF $N_D = 25$, $t = 0.4 \, \text{s}$; (c) IF $N_D = 50$, $t = 0.4 \, \text{s}$; (d) IF $N_D = 50$, $t = 0.5 \, \text{s}$; (e) IF $N_\text{D} = 75$, $t = 0.4 \, \text{s}$; (f) IF $N_\text{D} = 75$, $t = 0.448 \, \text{s}$; (g) IF $N_\text{D} = 100$, $t = 0.4 \, \text{s}$; (h) IF $N_D = 100$, $t = 0.42 \, \text{s}$.

30

5.2 Phase distribution

5.2.1 Interface thickness

To investigate the effect of mesh size on the interface compression in IF, the liquid volume fraction α is plotted along the horizontal midplane of the domain in Fig. 5 (a) for $D_0 = 500\,\mu m$ and three different resolutions. The comparison with the sharp interface profile in Fig. 5 (a) shows that the width of the smeared interface in IF decreases as N_D increases. For $N_D = 100$, the deviation from the sharp interface profile is already quite small. Similar profiles of the PFF order parameter over mesh resolution with fixed capillary width $\varepsilon = 10\,\mu m$ ($Cn = 0.02$) not shown here reveal that the symmetry with respect to the vertical midplane deviates for $N_C = 4$ while the profiles for $N_C = 6$ and 8 are symmetric and very similar. This indicates a lower threshold of diffuse interface resolution of six mesh cells in PFF to obtain reliable results, equal to $h \leq (2/3)\varepsilon$. When the interface resolution is fixed to $N_C = 8$, the increase of N_D and accordingly the decrease of ε and Cn lead to a smaller interface width, see Fig. 5 (b).
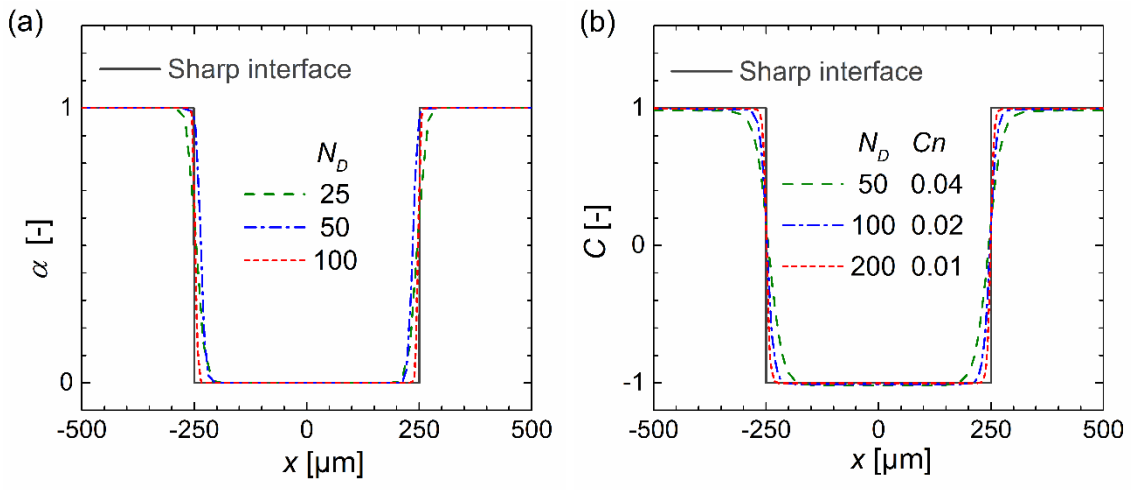
Fig. 5. Influence of mesh resolution on phase indicator profiles along the horizontal midplane ($D_0 = 500\,\mu m$) in (a) IF and (b) PFF ($N_C = 8$, variation of $N_D = D_0/h$ results in variation of $Cn = 2/N_D$ and $\varepsilon = Cn \cdot D_0$).

In Fig. 6, the interface thickness δ_{int} is plotted over grid resolution for $D_0 = 500\,\mu\text{m}$. For sharp interface methods, it is expected to scale with mesh size, which is the case for `IF`. The interface compression algorithm serves quite well in maintaining a ratio δ_{int}/h of about 1.8. In contrast, the interface thickness in `PFF` is related to the capillary width, here fixed to $\varepsilon = 10\,\mu\text{m}$. It decreases only slightly as N_D (and N_C) increases. Normalising the `PFF` interface thickness by the equilibrium width of the planar interface $L_{C,\text{planar}} = 4.164\varepsilon$ shows that δ_{int} approaches $L_{C,\text{planar}}$ as the resolution is increased while the Cahn number is fixed, see inset in Fig. 6. This is because the interface in a mesh cell tends to become planar as the ratio h/D_0 approaches zero.
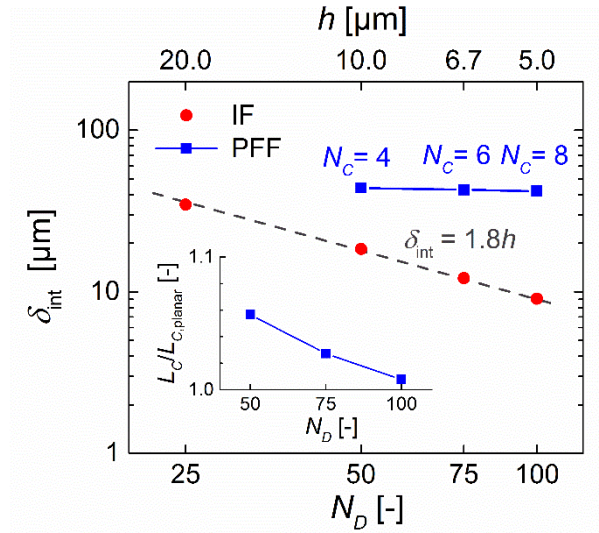
Fig. 6. Influence of mesh resolution on the interface thickness in `IF` and `PFF` (main graph) and on normalised interface thickness in `PFF` (inset).

5.2.2   *Bubble displacement*

Under the effect of the spurious currents, the bubble can deform (cf. Fig. 4 c-h) and, if the SC are not symmetric, the bubble might be displaced. Here, we investigate the influence of bubble size on the bubble displacement. Simulation results are considered

position-stable provided $x_B/h < 1$. Fig. 7 shows a displacement with IF up to almost

one bubble diameter decreasing with bubble size so that for $D_0 = 1000\,\mu\text{m}$ the bubble

position remains stable. PFF simulations on the other hand, always remain position-

stable and retain a displacement several orders of magnitude smaller than h. This is a

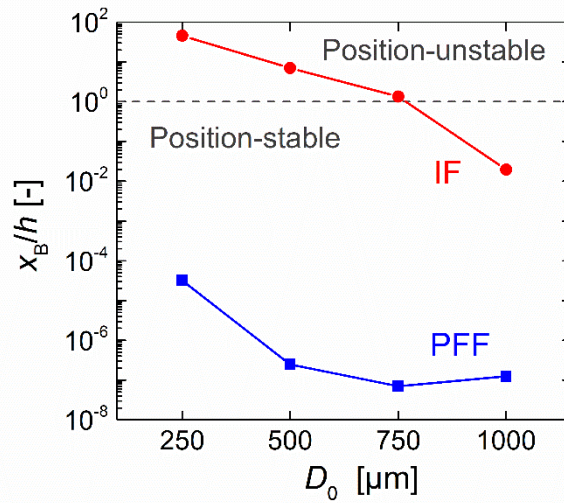consequence of symmetric and much smaller SC in PFF (cf. Fig. 4 and Section 5.4).

Fig. 7. Normalized bubble displacement x_B versus bubble diameter for fixed resolution

($N_D = 100$) in IF and PFF ($Cn = 0.02$, $N_C = 8$). Bubble position is unstable ($x_B > h$)

above the dashed horizontal line.

5.2.3 Bubble shape

To study the effect of mesh resolution on bubble shape, the normalised terminal mean

bubble diameter D_m and its standard deviation s_D are shown in Fig. 8. For IF, only the

results for $N_D = 25$ are included since for the finer grids the bubble shape is not steady

but oscillating in time (cf. Fig. 4). The relative error for the mean bubble diameter is

quite small (below 0.3% in IF and below 1% in PFF). In PFF, the mean bubble

diameter is consistently underestimated and its value is almost independent of mesh

size. The reason for this bubble shrinkage in `PFF` is discussed in Section 5.4. The results for s_D / D_0 in the inset of Fig. 8 show that the bubble circularity in `PFF` slightly increases with increase of N_D.
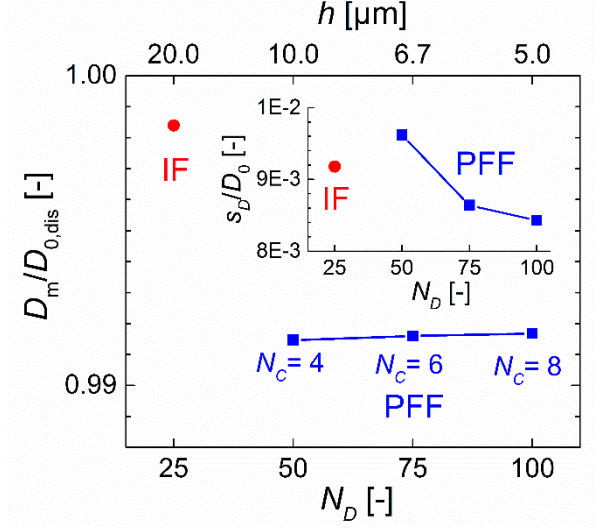

Fig. 8. Influence of mesh resolution on mean bubble diameter and its standard deviation (inset). Results of `PFF` ($Cn = 0.02$, $\varepsilon = 10\,\mu\text{m}$, $\chi = 0.1\,\text{m}\cdot\text{s/kg}$) and `IF` ($N_D = 25$ only) for $D_0 = 500\,\mu\text{m}$.

5.2.4 Bubble area

An important aspect in numerical simulations of interfacial flows is mass conservation which is, for the present test case, equivalent to conservation of bubble area. We therefore quantify mass conservation by the relative error in the bubble area $E_A := (A_{\text{final}} - A_{0,\text{dis}}) / A_{0,\text{dis}}$, where A_{final} is determined from isoline post-processing in ParaView® for $t = 0.4\,\text{s}$. The values for E_A are listed in Table 2. `IF` exhibits the excellent mass conservation properties of the VOF method, especially for high grid resolution. The very small identical error values for the two finest resolutions indicate that the interpolation error in determining the bubble area via the isoline post-processing

procedure is sufficiently small. While the bubble shape in the IF simulation with

$N_D = 75$ deviates notably from the spherical shape at $t = 0.4$ s (cf. Fig. 4 e), the bubble

area is well conserved throughout the simulation. For PFF, the bubble area deviates

more (Table 2). When the grid resolution is fixed ($N_D = 100$, $N_C = 8$, $Cn = 0.02$) the

bubble size has an influence on mass loss as well, see Table 3. PF computations

generally exhibit a drop or bubble shrinkage while globally conserving the order

parameter [44]. In all present PFF simulations, the integral of C over the computational

domain is indeed constant to eight significant digits. While "total mass" is thus

conserved, the area enclosed by the interface is not conserved.

Table 2 Area conservation error E_A (%) for base case $D_0 = 500\,\mu\mathrm{m}$.

N_D	25	50	75	100
interFoam	-0.44	-0.06	0.01	0.01
phaseFieldFoam		-1.61	-1.64	-1.65

Table 3 Area conservation error E_A (%) for varying bubble diameter ($N_D = 100$).

D_0 [μm]	250	500	750	1000
interFoam	0.03	0.01	0.04	0.04
phaseFieldFoam		-1.65	-1.42	-1.26

The apparent area/mass loss in PFF is associated with the order parameter profile.

Initially, the order parameter is in the range $C_{\min,0} \leq C \leq C_{\max,0}$ where

$C_{\max,0} = -C_{\min,0} = 1$. The discrimination between the two phases is based on

$C_{\text{mean},0} = (C_{\text{max},0} + C_{\text{min},0})/2 = 0$. Since no special measures are taken to guarantee the boundedness of the order parameter, both its minimum and maximum deviate from the initial values over time. This corresponds to a shift of the order parameter for the bulk phases, see sketch in Fig. 9 (a). If the phase discrimination is based on $C_{\text{mean},0}$, this goes along with an apparent mass conservation error. To quantify the shift in the order parameter in the present simulations, we define for the liquid phase

$\delta C_{\text{L}} = C_{\text{max},0} - C_{\text{max}} = 1 - C_{\text{max}}$ and for the gas phase $\delta C_{\text{G}} = C_{\text{min},0} - C_{\text{min}} = -1 - C_{\text{min}}$.

Using an energy argument and assuming an equal shift in both bulk components, Yue et al. [44] estimated the shift for a 2D circular fluid particle as

$$\delta C = \pm \frac{\sqrt{2}}{3} Cn, \tag{16}$$

where the plus sign applies for a "drop" (with $C = 1$ inside) and the minus sign for a "bubble" (with $C = -1$ inside).
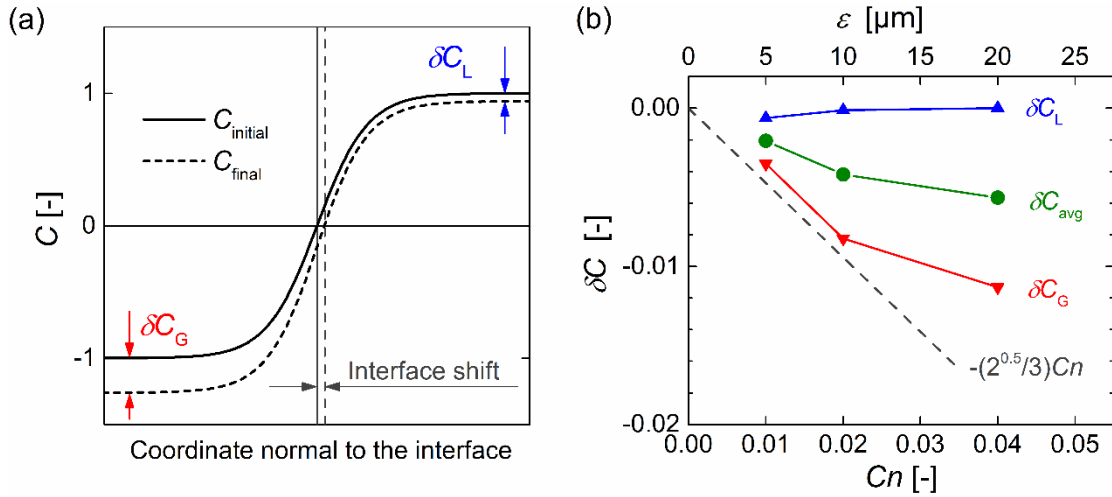

Fig. 9. (a) Sketch of the shift of C and (b) influence of Cahn number on this shift in PPF simulations ($D_0 = 500\,\mu\text{m}$, $N_C = 8$, $M = 2.5\times10^{-12}\,\text{m}^3\text{s/kg}$).

36

Fig. 9 (b) compares the evaluated values for δC_{L} and δC_{G} with Eq. (16) for three

different Cahn numbers. As expected, the values are negative for the present bubble

cases. However, δC_{L} and δC_{G} considerably differ in magnitude, which is in contrast to

the assumption made in [44]. While the magnitude of δC_{L} is very small and almost

zero, the magnitude of δC_{G} is much larger. For the two smaller values of Cn, δC_{G} is

close to Eq. (16) with negative sign. As a consequence of the small values of δC_{L}, the

average $(\delta C_{\mathrm{L}} + \delta C_{\mathrm{G}})/2$ is smaller than the estimation by Yue et al. [44]. Nevertheless,

Eq. (16) can be used as a reasonable upper limit for the error in δC. Clarifying the

reasons for the asymmetry of the order parameter shift in both phases and for the very

small values of δC_{L} requires further research. Notably, using the actual value of C_{mean}

instead of $C_{\mathrm{mean},0} = 0$ for discriminating the phases, yields even smaller bubble

diameters and therefore even worse results for bubble area conservation. We remark

that for better preserving the enclosed area, recently a PF model with interfacial

correction term was proposed [97].

Fig. 10 shows the influence of mobility on bubble shrinkage plotting the normalised

bubble diameter over Cahn number with constant and variable M. As expected, both

bubble shrinkage and mass loss decrease with decreasing Cn. This trend is amplified by

simultaneously decreasing the mobility. Overall, one can conclude that `PFF` shows

notable errors in mass conservation at higher Cahn numbers, but conserves mass

reasonably well for $Cn \leq 0.01$. This suggests that Cn should be as small as possible.

However, low Cahn numbers require fine grids, which significantly increase the CPU

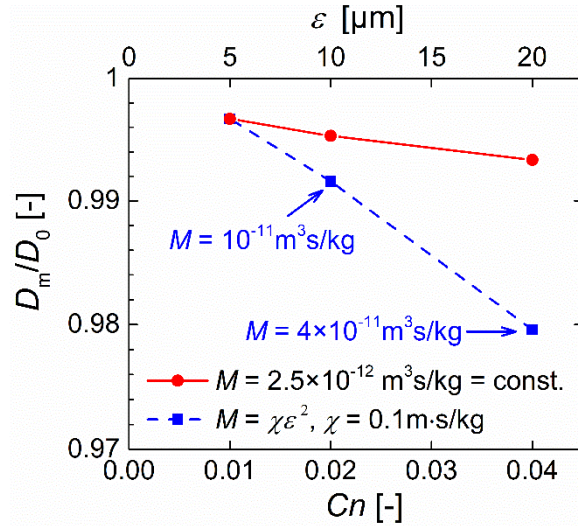time on uniform meshes. Thus, local dynamic adaptive mesh refinement is

recommended.

Fig. 10. Influence of Cahn number on normalised terminal mean bubble diameter for PFF simulations with fixed and variable mobility ($D_0 = 500\,\mu\text{m}$, $N_C = 8$).

5.3 Pressure

5.3.1 Pressure profiles

In order to quantify the accuracy in pressure, we compare the numerical results with the pressure jump from the Young-Laplace equation. We first consider the diameter $D_0 = 500\,\mu\text{m}$ yielding a Laplace pressure jump of $\Delta p_{\text{exact}} = 291.4\,\text{Pa}$. For better graphical comparison, the pressure profiles are shifted so that the pressure at the boundaries of the computational domain is zero.

Fig. 11 (a) displays IF pressure profiles along the horizontal midplane for three different mesh resolutions. The comparison with the exact pressure profile in the sharp interface limit shows that IF underestimates the pressure jump by more than 10%, even with the finest resolution. The underestimation is the largest for case $N_D = 50$ where the bubble deformation is large at $t = 0.4\,\text{s}$. However, even for the case with $N_D = 25$ where the bubble deformation is small (Fig. 4 b) the pressure is notably underestimated.

Fig. 11 (b) shows pressure profiles obtained with PFF for three different values of N_D under fixed interface resolution ($N_C = 8$) and variable Cahn number $Cn = 2/N_D$. The pressure jump is slightly overestimated for $Cn = 0.04$ and 0.02 with the deviation decreasing with lower Cn. Since the interface thickness decreases as well, the numerical pressure profile approaches the sharp interface limit as Cn is decreasing.
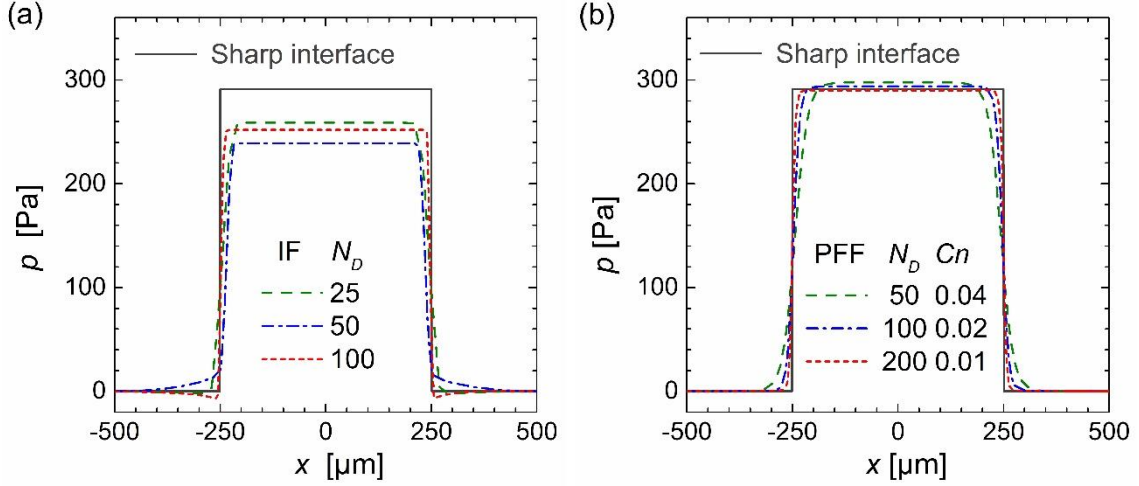

Fig. 11. Influence of mesh resolution on pressure profiles along the horizontal midplane for $D_0 = 500\,\mu m$: (a) IF, (b) PFF ($N_C = 8$, variation of N_D results in variation of $Cn = 2/N_D$, $\varepsilon = Cn \cdot D_B$ and $M = \chi \varepsilon^2$, $\chi = 0.1\,m \cdot s/kg$).

5.3.2 Pressure jump

For a quantitative assessment of the pressure jump, the pressure in the liquid and gas domains is averaged (cf. Section 3.5.4). Fig. 12 displays the normalised pressure jump $\Delta p_{num}/\Delta p_{exact}$ for the IF simulations in Fig. 11 a) and PFF simulations with fixed Cahn number ($Cn = 0.02$). The relative error in PFF is then less than 0.6% but more than 10% in IF. Pressure errors of similar magnitude for IF are reported in [69, 73, 85]. Notably, with both codes the error slightly increases with mesh refinement.
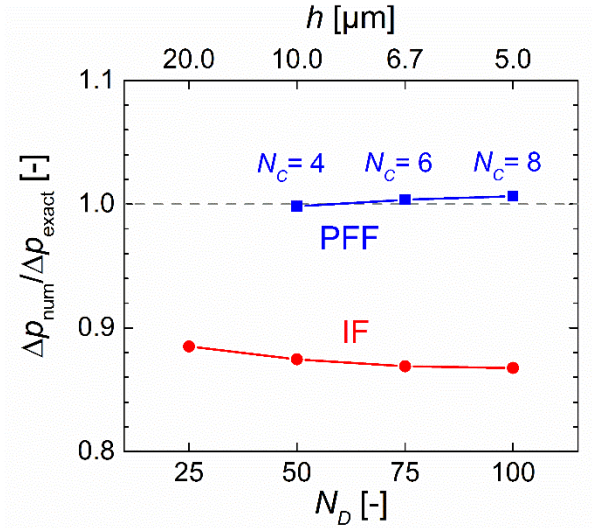
Fig. 12. Influence of mesh resolution on normalised pressure jump ($D_0 = 500\,\mu\text{m}$) in `IF` and `PFF` ($Cn = 0.02$, $\varepsilon = 10\,\mu\text{m}$, $\chi = 0.1\,\text{m}\cdot\text{s/kg}$).

Fig. 13 compares the numerical pressure jump of bubbles with different diameter with the Young-Laplace law. While the `PFF` results agree well with the Young-Laplace law, the `IF` deviation is obvious. Furthermore, the slope of the `IF` results deviates strikingly from 2σ of the Young-Laplace law. The good performance of the PF method is in agreement with the theoretical analysis of Antanovskii [98]. It also supports the statement of Jacqmin [26] that the error in pressure jump due to interface curvature when computing σ from Eq. (7) is small, provided interface thickness times curvature is low. For the PFF simulations in Fig. 13 it is $\varepsilon\kappa = 2\varepsilon / D_0 = 2Cn = 0.04$.
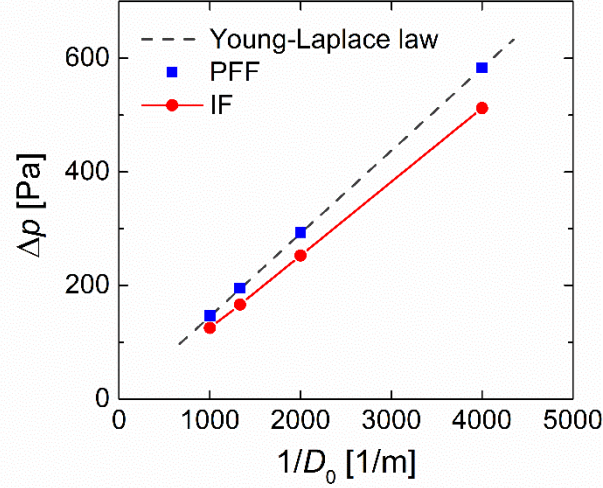
Fig. 13. Influence of bubble diameter on pressure jump for fixed bubble resolution ($N_D = 100$) in `IF` and `PFF` ($Cn = 0.02$, $N_C = 8$).

5.4 Spurious currents

After an initial decay, the spurious currents in `IF` fluctuate around a time-independent mean value. The `PFF` results show no such fluctuations. However, for some cases no constant value has been reached at the end of the simulation. The analysis is thus performed on averaged values of U_{sc} over the period $t = 0.3 - 0.4\,\mathrm{s}$.

For $D_0 = 500\,\mu\mathrm{m}$, both solvers exhibit a roughly constant U_{sc} over grid resolution (Fig. 14). For `IF`, the spurious currents are of magnitude $O(1\,\mathrm{m/s})$ while for `PFF` they remain at $O(10^{-5}\,\mathrm{m/s})$. In contrast to the test cases of Albadawi et al. [70] and Yokoi [76] from Section 4, the `PFF` results for the SC do not converge with grid refinement any more. From U_{sc} in Fig. 14, the capillary number of the SC can be computed. Taking the mean value of the liquid and gas viscosities for this purpose yields $Ca_{sc} = U_{sc}(\mu_L + \mu_G)/2\sigma \approx 7 \times 10^{-3}$ for `IF`, a value comparable to that found for the Albadawi test case in Fig. 2. For `PFF`, the corresponding capillary number is about 7×10^{-8} and thus even smaller as for the Albadawi test case.
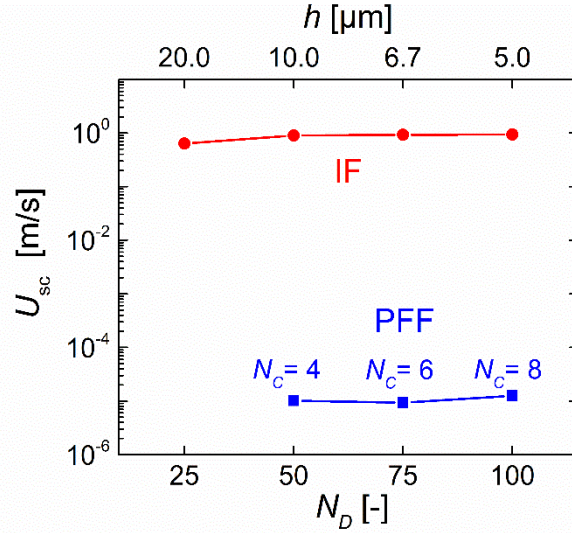
41

Fig. 14. Influence of mesh resolution on maximum spurious currents for $D_0 = 500\,\mu\text{m}$ in `IF` and `PFF` ($Cn = 0.02$, $\varepsilon = 10\,\mu\text{m}$, $\chi = 0.1\,\text{m} \cdot \text{s/kg}$).

Fig. 15 shows the influence of the bubble diameter on SC for fixed bubble resolution ($N_D = 100$). In the `PFF` simulations, $Cn = 0.02$, $N_C = 8$ and $\chi = 0.1\,\text{m} \cdot \text{s/kg}$ are fixed as well. The capillary width and the mobility vary as $\varepsilon = Cn \cdot D_0$ and $M = \chi \varepsilon^2$. Similar to Fig. 14, `IF` yields large SC of about $1\,\text{m/s}$ independent on bubble size. For `PFF`, U_{sc} is about $10^{-5}\,\text{m/s}$ for $D_0 \geq 500\,\mu\text{m}$ but increases to $0.1\,\text{m/s}$ for $D_0 = 250\,\mu\text{m}$. A potential explanation for this large latter value may be offered by the theoretical investigation of Yue et al. [44]. The authors showed that in the PF method a critical initial diameter $D_{0,\text{crit}} = (\sqrt{6} A_\Omega \varepsilon / 8\pi)^{1/3}$ exists, below which a drop finally disappears. For the simulations in Fig. 15, the area of the computational domain is $A_\Omega = 4D_0^2$ and $\varepsilon = 0.02 D_0$. This yields $D_0 / D_{0,\text{crit}} \approx 5$ for all simulations, which appears sufficiently large. Instead, it turned out that the large SC for case $D_0 = 250\,\mu\text{m}$ are related to the time step size. The criterion in Eq. (13) yields $\Delta t_{\text{Aland}} = 1.14\,\mu\text{s}$ for this case. Decreasing Δt_{max} by a factor of ten from $5\,\mu\text{s}$ to $0.5\,\mu\text{s}$

decreases the SC by about four orders of magnitude, see Fig. 15. This indicates that the capillary time step criterion in Eq. (13) is relevant for `PFF` as well.
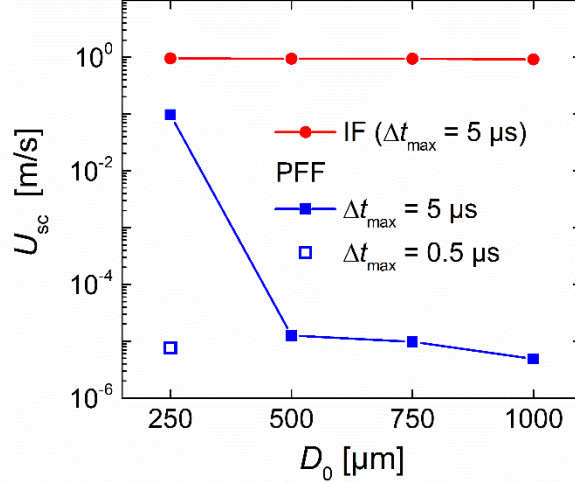

Fig. 15. Influence of bubble diameter on spurious currents for fixed bubble resolution ($N_D = 100$) in `IF` and `PFF` ($Cn = 0.02$, $N_C = 8$).

6 Conclusion

In this article, we evaluated two numerical methods implemented in OpenFOAM® concerning their suitability for interface resolving simulations of submillimetre air-bubbles in water. The code `interFoam` implements an algebraic volume-of-fluid method for a nominally sharp interface with standard continuum surface force and curvature computations, whereas `phaseFieldFoam` is based on the phase-field method with diffuse interface representation with capillary term in free energy formulation.

A nominally static circular bubble surrounded by quiescent liquid in absence of gravity serves as test case. The two-dimensional simulations explore the impact in variation of mesh size (h) of the uniform grid and bubble size. Evaluating the bubble

shape, mass conservation, the Young-Laplace pressure jump and the magnitude of spurious currents serve as measures for the accuracy of the solvers.

A reference is drawn to investigations in literature by examining the solvers on two test cases with simplified conditions, i.e. matched density/viscosity and an artificially large inviscid drop. The code `interFoam` reveals spurious currents not decreasing with mesh resolution and several orders of magnitude larger than in `phaseFieldFoam`, where they decrease with second order convergence. This convergence is attributed to the absence of curvature computation, the interface thickness being controlled by the capillary width (ε) independent from mesh resolution, and an easy to achieve balanced discretisation between pressure gradient and capillary term.

In the numerically challenging case of a submillimetre air bubble in quiescent water, spurious currents remain independent on the mesh size loosing second order convergence in `phaseFieldFoam`. However, there, the magnitude of the spurious currents remains five orders in magnitude below `interFoam`. The large asymmetric spurious currents in `interFoam` significantly displace and deform the bubble especially at higher resolution where the shape is oscillating, while the bubble remains always circular and preserving its initial position in `phaseFieldFoam`. The latter code predicts the Laplace pressure jump below an error of 1% while the former underestimates by about 13%. The code `interFoam` exhibits very low errors in mass conservation below 0.1% on fine grids whereas `phaseFieldFoam` shrinks the bubble in the course of the simulations while globally conserving the order parameter. This phenomenon is well known in literature and results from a shift of the order parameter values in the bulk phases. With `phaseFieldFoam`, the mass conservation error at

Cahn number 0.02 on very fine grids is about 1.6%, which can be reduced by decreasing the Cahn number, i.e. the capillary width. At the same time, it is essential that the diffuse interface region is well resolved. Thus, a much finer resolution is required in `phaseFieldFoam` for obtaining good mass conservation as compared to `interFoam`.

Concluding, despite its superior mass conservation properties the standard `interFoam` solver lacks the accuracy to predict reasonable physics for a bubble in microfluidic systems. Comparison with literature shows that its performance might be significantly improved by making use of height functions in the curvature estimation. However, the supposed benefits are expected to reach performances still worse than geometrical VOF approaches that reconstruct the interface. The solver `phaseFieldFoam` exhibits sufficient accuracy providing the Cahn number is below about 0.01 and the diffuse interface is well resolved ($h \leq \varepsilon / 2$). These requirements lead on static uniform grids to high computational costs for 3D simulations. Practical engineering computations with `phaseFieldFoam` thus require local dynamic adaptive mesh refinement in the diffuse interface region.

Though the present study focused on the effect of grid resolution, some conclusions concerning temporal resolution can be drawn as well. The time step criterion derived in [69] for matched fluid properties and suggested for accurate position-stable simulations with `interFoam` cannot be directly transferred to the present very demanding test case of submillimetre air bubbles in water with large density contrast. For `phaseFieldFoam`, the present combination of a Courant time step restriction with an upper limit for the time step size serves quite well for most cases. However, suppression

of spurious currents in simulations using very small values of the capillary width

requires incorporation of the capillary time step restriction proposed in [92].

Conflict of Interest

The authors declare that they have no conflict of interest.

References

[1] S.Y. Teh, R. Lin, L.H. Hung, A.P. Lee, Lab Chip 8 (2008) 198-220.
[2] H. Song, D.L. Chen, R.F. Ismagilov, Angew. Chem. Int. Ed. 45 (2006) 7336-7356.
[3] F. Schuler, M. Trotter, M. Geltman, F. Schwemmer, S. Wadle, E. Dominguez-Garrido, M. Lopez, C. Cervera-Acedo, P. Santibanez, F. von Stetten, R. Zengerle, N. Paust, Lab Chip 16 (2016) 208-216.
[4] Y. Wang, D. Lee, L.S. Zhang, H. Jeon, J.E. Mendoza-Elias, T.A. Harvat, S.Z. Hassan, A. Zhou, D.T. Eddington, J. Oberholzer, Biomed. Microdevices 14 (2012) 419-426.
[5] M.J. Jensen, G. Goranovic, H. Bruus, J. Micromech. Microeng. 14 (2004) 876-883.

[6] H. Chio, M.J. Jensen, X.L. Wang, H. Bruus, D. Attinger, J. Micromech. Microeng. 16 (2006) 143-149.

[7] J. Kohnle, G. Waibel, R. Cernosa, M. Storz, H. Ernst, H. Sandmaier, T. Strobelt, R. Zengerle, A unique solution for preventing clogging of flow channels by gas bubbles, Fifteenth IEEE Int. Conf. Micro Electro Mechanical Systems (MEMS), 2002, pp. 77-80.

[8] J. Xu, R. Vaillant, D. Attinger, Microfluid. Nanofluid. 9 (2010) 765-772.

[9] H. van Lintel, G. Mernier, P. Renaud, Micromachines 3 (2012) 218-224.

[10] F.P. Bretherton, J. Fluid Mech. 10 (1961) 166-188.

[11] K. Muramatsu, Y. Youn, Y. Han, Y. Hasegawa, N. Shikazono, Int. J. Heat Fluid Flow 54 (2015) 77-86.

[12] M.B. de Azevedo, D. dos Santos, J.L.H. Faccini, J. Su, Int. J. Multiphase Flow 88 (2017) 133-141.

[13] A.A. Saha, S.K. Mitra, J. Colloid Interface Sci. 339 (2009) 461-480.

[14] J.H. Snoeijer, B. Andreotti, Annu. Rev. Fluid Mech. 45 (2013) 269-292.

[15] M. Huber, F. Keller, W. Sackel, M. Hirschler, P. Kunz, S.M. Hassanizadeh, U. Nieken, J. Comput. Phys. 310 (2016) 459-477.

[16] C. Priest, S. Herminghaus, R. Seemann, Appl. Phys. Lett. 89 (2006).

[17] Y.C. Tan, Y.L. Ho, A.P. Lee, Microfluid. Nanofluid. 3 (2007) 495-499.

[18] L. Mazutis, A.D. Griffiths, Lab Chip 12 (2012) 1800-1806.

[19] V. Tesar, Chem. Eng. Sci. 116 (2014) 843-848.

[20] T.T. Fu, Y.G. Ma, Chem. Eng. Sci. 135 (2015) 343-372.

[21] A. Beskok, G.E. Karniadakis, J. Thermophys Heat Transfer 8 (1994) 647-655.

[22] H. Marschall, K. Hinterberger, C. Schuler, F. Habla, O. Hinrichsen, Chem. Eng. Sci. 78 (2012) 111-127.

[23] M. Wörner, Microfluid. Nanofluid. 12 (2012) 841-886.

[24] C.W. Hirt, B.D. Nichols, J. Comput. Phys. 39 (1981) 201-225.

[25] S. Osher, R.P. Fedkiw, Level set methods and dynamic implicit surfaces, Springer, Berlin, London, 2003.

[26] D. Jacqmin, J. Comput. Phys. 155 (1999) 96-127.

[27] S.O. Unverdi, G. Tryggvason, J. Comput. Phys. 100 (1992) 25-37.

[28] H. Huang, M. Sukop, X. Lu, Multiphase Lattice Boltzmann Methods: Theory and Application, Wiley-Blackwell, Hoboken, 2015.

[29] Z.B. Wang, R. Chen, H. Wang, Q. Liao, X. Zhu, S.Z. Li, Appl. Math. Model. 40 (2016) 9625-9655.

[30] W.F. Noh, P. Woodward, SLIC (Simple Line Interface Calculation), Lecture Notes in Physics, Springer, New York, 1976, pp. 330-340.

[31] D.L. Youngs, Time-dependent multi-material flow with large fluid distortion, in: K.W. Morton, M.J. Baines (Eds.) Numerical methods for Fluid Dynamics, Academic Press, New York, 1982, pp. 273-285.

[32] W.J. Rider, D.B. Kothe, J. Comput. Phys. 141 (1998) 112-152.

[33] B.G.M. van Wachem, J.C. Schouten, AlChE J. 48 (2002) 2744-2753.

[34] J. Roenby, H. Bredmose, H. Jasak, Royal Society Open Science 3 (2016) 160405.

[35] T. Marić, H. Marschall, D. Bothe, J. Comput. Phys. (2018).

[36] O. Ubbink, R.I. Issa, J. Comput. Phys. 153 (1999) 26-50.

[37] S. Muzaferija, M. Peric, Computation of flows using interface-tracking and interface-capturing methods, in: O. Mahrenholtz, M. Markiewicz (Eds.) Nonlinear Water Wave Interaction, WIT Press, Southampton, 1998, pp. 59-100.

[38] K.K. So, X.Y. Hu, N.A. Adams, J. Comput. Phys. 230 (2011) 5155-5177.

[39] D.A. Cassidy, J.R. Edwards, M. Tian, J. Comput. Phys. 228 (2009) 5628-5649.

[40] V.R. Gopala, B.G.M. van Wachem, Chem. Eng. J. 141 (2008) 204-221.

[41] D.M. Anderson, G.B. McFadden, A.A. Wheeler, Annu. Rev. Fluid Mech. 30 (1998) 139-165.

[42] J.W. Cahn, J.E. Hilliard, J. Chem. Phys. 28 (1958) 258-267.

[43] S.M. Allen, J.W. Cahn, Acta Metall. 27 (1979) 1085-1095.

[44] P. Yue, C. Zhou, J.J. Feng, J. Comput. Phys. 223 (2007) 1-9.

[45] J. Kim, Commun. Comput. Phys. 12 (2012) 613-661.

[46] H.G. Weller, A new approach to VOF-based interface capturing methods for incompressible and compressible flow, Tech. Rep. TR/HGW/07, OpenCFD Ltd., 2006.

[47] X. Cai, H. Marschall, M. Wörner, O. Deutschmann, Chem. Eng. Technol. 38 (2015) 1985-1992.

[48] H. Marschall, L. Cornolti, X. Cai, M. Wörner, (2018) In preparation.

[49] B. Lafaurie, C. Nardone, R. Scardovelli, S. Zaleski, G. Zanetti, J. Comput. Phys. 113 (1994) 134-147.

[50] M.M. Francois, S.J. Cummins, E.D. Dendy, D.B. Kothe, J.M. Sicilian, M.W. Williams, J. Comput. Phys. 213 (2006) 141-173.

[51] J.U. Brackbill, D.B. Kothe, C. Zemach, J. Comput. Phys. 100 (1992) 335-354.

[52] Y. Renardy, M. Renardy, J. Comput. Phys. 183 (2002) 400-421.

[53] H. Weking, J. Schlottke, M. Boger, P. Rauschenberger, B. Weigand, C.-D. Munz, DNS of Rising Bubbles Using VOF and Balanced Force Surface Tension, in: M. Resch, K. Benkert, X. Wang, M. Galle, W. Bez, H. Kobayashi, S. Roller (Eds.) High Performance Computing on Vector Systems 2010, Springer, Berlin, Heidelberg, 2010, pp. 171-184.

[54] S.J. Cummins, M.M. Francois, D.B. Kothe, Comput. Struct. 83 (2005) 425-434.

[55] B.B.M. Kassar, J.N.E. Carneiro, A.O. Nieckele, Comput. Phys. Commun. 222 (2018) 189-208.

[56] T. Abadie, J. Aubin, D. Legendre, J. Comput. Phys. 297 (2015) 611-636.

[57] S. Popinet, J. Comput. Phys. 228 (2009) 5838-5866.

[58] S. Bnà, S. Manservisi, R. Scardovelli, P. Yecko, S. Zaleski, Comput. Phys. Commun. 200 (2016) 291-299.

[59] S. Popinet, Annu. Rev. Fluid Mech. 50 (2018) 49-75.

[60] P.C. Hohenberg, B.I. Halperin, Rev. Mod. Phys. 49 (1977) 435-479.

[61] J. Lowengrub, L. Truskinovsky, Proc. R. Soc. London, Ser. A 454 (1998) 2617-2654.

[62] M. De Menech, Physical Review E 73 (2006) 031505.

[63] J. Kim, J. Comput. Phys. 204 (2005) 784-804.

[64] Q.W. He, N. Kasagi, Fluid Dyn. Res. 40 (2008) 497-509.

[65] H.G. Lee, J. Kim, Int. J. Numer. Meth. Eng. 91 (2012) 269-288.

[66] I. Halliday, S.V. Lishchuk, T.J. Spencer, K. Burgin, T. Schenkel, Comput. Phys. Commun. 219 (2017) 286-296.

[67] M. Zhang, X.-L. Deng, J. Comput. Phys. 302 (2015) 469-484.

[68] E. Gros, G.R. Anjos, J.R. Thome, Int. J. Numer. Methods Fluids 86 (2018) 201-217.

[69] S.S. Deshpande, L. Anumolu, M.F. Trujillo, Computational Science & Discovery 5 (2012) 014016.

[70] A. Albadawi, D.B. Donoghue, A.J. Robinson, D.B. Murray, Y.M.C. Delaure, Int. J. Multiphase Flow 53 (2013) 11-28.

[71] Z.Y. Guo, D.F. Fletcher, B.S. Haynes, Appl. Math. Model. 39 (2015) 4665-4686.

[72] M. Magnini, B. Pulvirenti, J.R. Thome, Appl. Math. Model. 40 (2016) 6811-6830.

[73] C. Bilger, M. Aboukhedr, K. Vogiatzaki, R.S. Cant, J. Comput. Phys. 345 (2017) 665-686.

[74] M. Aboukhedr, A. Georgoulas, M. Marengo, M. Gavaises, K. Vogiatzaki, Computers & Fluids 165 (2018) 13-32.

[75] D.J.E. Harvie, M.R. Davidson, M. Rudman, Appl. Math. Model. 30 (2006) 1056-1066.

[76] K. Yokoi, J. Comput. Phys. 278 (2014) 221-228.

[77] F. Denner, D.R. van der Heul, G.T. Oud, M.M. Villar, A.D. Neto, B.G.M. van Wachem, Int. J. Multiphase Flow 61 (2014) 37-47.

[78] M. Meier, G. Yadigaroglu, B.L. Smith, Eur. J. Mech. B-Fluids 21 (2002) 61-73.

[79] S.T. Zalesak, J. Comput. Phys. 31 (1979) 335-362.

[80] R.I. Issa, J. Comput. Phys. 62 (1986) 40-65.

[81] S.V. Patankar, D.B. Spalding, Int. J. Heat Mass Transfer 15 (1972) 1787-&.

[82] A.Q. Raeini, M.J. Blunt, B. Bijeljic, J. Comput. Phys. 231 (2012) 5653-5668.

[83] D.A. Hoang, V. van Steijn, L.M. Portela, M.T. Kreutzer, C.R. Kleijn, Computers & Fluids 86 (2013) 28-36.

[84] M. Binz, W. Rohlfs, R. Kneer, Fluid Dyn. Res. 46 (2014).

[85] A. Ferrari, M. Magnini, J.R. Thome, Int. J. Multiphase Flow 91 (2017) 276-295.

[86] P.T. Yue, J.J. Feng, C. Liu, J. Shen, J. Fluid Mech. 515 (2004) 293-317.

[87] W. Villanueva, G. Amberg, Int. J. Multiphase Flow 32 (2006) 1072-1086.

[88] X. Cai, M. Wörner, H. Marschall, O. Deutschmann, Catal. Today 273 (2016) 151-160.

[89] X. Cai, M. Wörner, H. Marschall, O. Deutschmann, Emis. Contr. Sci. Technol. 3 (2017) 289-301.

[90] V. Fink, X. Cai, A. Stroh, R. Bernard, J. Kriegseis, B. Frohnapfel, H. Marschall, M. Wörner, Int. J. Heat Fluid Flow 70 (2018) 271-278.

[91] C. Galusinski, P. Vigneaux, J. Comput. Phys. 227 (2008) 6140-6164.

[92] S. Aland, J. Comput. Phys. 262 (2014) 58-71.

[93] S. Popinet, S. Zaleski, Int. J. Numer. Methods Fluids 30 (1999) 775-793.

[94] M.W. Williams, D.B. Kothe, E.G. Puckett, Accuracy and convergence of continuum surface-tension models, in: W. Shyy, R. Narayanan (Eds.) Fluid Dynamics at Interfaces, Cambridge University Press, Cambridge, UK, 1999, pp. 294-305.

[95] D. Gerlach, G. Tomar, G. Biswas, F. Durst, Int. J. Heat Mass Transfer 49 (2006) 740-754.

[96] E.G. Puckett, A.S. Almgren, J.B. Bell, D.L. Marcus, W.J. Rider, J. Comput. Phys. 130 (1997) 269-282.

[97] Y.B. Li, J.I. Choi, J. Kim, Commun. Nonlinear. Sci. 30 (2016) 84-100.

[98] L.K. Antanovskii, Phys. Fluids 7 (1995) 747-753.